

# Solar coronal heating from small-scale magnetic braids

L. P. Chitta<sup>1</sup>, H. Peter<sup>1</sup>, S. Parenti<sup>2</sup>, D. Berghmans<sup>3</sup>, F. Auchère<sup>2</sup>, S. K. Solanki<sup>1,4</sup>, R. Aznar Cuadrado<sup>1</sup>, U. Schühle<sup>1</sup>, L. Teriaca<sup>1</sup>, S. Mandal<sup>1</sup>, K. Barczynski<sup>5,6</sup>, É. Buchlin<sup>2</sup>, L. Harra<sup>5,6</sup>, E. Kraaikamp<sup>3</sup>, D. M. Long<sup>7</sup>, L. Rodriguez<sup>3</sup>, C. Schwanitz<sup>5,6</sup>, P. J. Smith<sup>7</sup>, C. Verbeek<sup>3</sup>, A. N. Zhukov<sup>3,8</sup>, W. Liu<sup>9,10</sup>, and M. C. M. Cheung<sup>9</sup>

<sup>1</sup> Max-Planck-Institut für Sonnensystemforschung, Justus-von-Liebig-Weg 3, 37077 Göttingen, Germany  
e-mail: chitta@mps.mpg.de

<sup>2</sup> Université Paris-Saclay, CNRS, Institut d'astrophysique spatiale, 91405, Orsay, France

<sup>3</sup> Solar-Terrestrial Centre of Excellence - SIDC, Royal Observatory of Belgium, Ringlaan -3- Av. Circulaire, 1180 Brussels, Belgium

<sup>4</sup> School of Space Research, Kyung Hee University, Yongin, Gyeonggi 446-701, Republic of Korea

<sup>5</sup> Physikalisch-Meteorologisches Observatorium Davos, World Radiation Center, 7260 Davos Dorf, Switzerland

<sup>6</sup> ETH-Zürich, Wolfgang-Pauli-Str. 27, 8093 Zürich, Switzerland

<sup>7</sup> UCL-Mullard Space Science Laboratory, Holmbury St. Mary, Dorking, Surrey RH5 6NT, UK

<sup>8</sup> Skobeltsyn Institute of Nuclear Physics, Moscow State University, 119992 Moscow, Russia

<sup>9</sup> Lockheed Martin Solar and Astrophysics Laboratory, 3251 Hanover Street, Building 252, Palo Alto, CA 94304, USA

<sup>10</sup> Bay Area Environmental Research Institute, NASA Research Park, Moffett Field, CA 94035, USA

Received ; accepted

## ABSTRACT

Relaxation of braided coronal magnetic fields through reconnection is thought to be a source of energy to heat plasma in active region coronal loops. However, observations of active region coronal heating associated with untangling of magnetic braids remain sparse. One reason for this paucity could be the lack of coronal observations with sufficiently high spatial and temporal resolution to capture this process in action. Using new high spatial resolution (250–270 km on the Sun) and high cadence (3–10 s) observations from the Extreme Ultraviolet Imager (EUI) on board Solar Orbiter we observed untangling of small-scale coronal braids in different active regions. The untangling is associated with impulsive heating of the gas in these braided loops. We assess that coronal magnetic braids overlying cooler chromospheric filamentary structures are perhaps more common. Furthermore, our observations show signatures of both spatially coherent and intermittent coronal heating during relaxation of magnetic braids. Our study reveals the operation of both more gentle and impulsive modes of magnetic reconnection in the solar corona.

**Key words.** Sun: corona — Sun: magnetic fields — Magnetic reconnection — Plasmas

## 1. Introduction

One of the widely invoked models to explain the million Kelvin solar corona is through magnetic braiding (Parker 1972, 1983). In this scenario, magnetic footpoints of coronal loops are slowly stressed and randomly moved by photospheric convective motions, leading to braiding of magnetic field in the corona, i.e. wrapping of field lines around each other. Current sheets form at these braids due to magnetic field misalignment. These current sheets dissipate impulsively, on timescales shorter than typical coronal cooling timescales, through reconnection to produce storms of nanoflares all along the loops, which then intermittently heat the coronal plasma to the observed temperatures in excess of 1 MK (Parker 1988; Klimchuk 2006). This nanoflare heating from untangling of braids is postulated to be central to explaining active region loops that reach temperatures above 2 MK. Photospheric convective motions also excite magnetohydrodynamic (MHD) waves, but observations and models show that these waves are not energetic enough to power such hot active region coronal loops (McIntosh et al. 2011; Van Doorselaere et al. 2020). However, their contribution cannot be ruled out (e.g. Asgari-Targhi et al. 2019), because at the photospheric level waves carry enough Poynting flux to heat the active region corona. The open issue here is whether this energy gets chan-

neled into the corona and how waves could efficiently dissipate the energy to heat coronal plasma (Van Doorselaere et al. 2020).

Three-dimensional (3D) MHD models of the solar atmosphere do produce 1–4 MK hot active region loops in the corona (e.g. Gudiksen & Nordlund 2002; Warnecke & Peter 2019). Here the heating is generally ascribed to the slow stressing of photospheric footpoints. High-resolution 3D MHD simulations that include self-consistent convective motions induce both slow stressing of footpoints and waves into the corona (Breu et al. 2022). However, partition of energy flux channeled into the corona by these two modes, in such a high-resolution model, has not yet been fully explored.

Overall, the observational validation of coronal heating through nanoflares as proposed by Parker (1988), remains elusive. In particular, spatial, temporal, and thermal regimes at which magnetic braiding and the associated nanoflare heating operate in the solar corona are observationally not well constrained.

One of the early, but occasional indications of magnetic braiding or wrapping of loops in the corona was through TRACE 171 Å filter images in the extreme ultraviolet (EUV) (Schrijver et al. 1999). However, van Ballegoijen et al. (2011) argued that the observed TRACE cases of braiding were ambiguous (see also Pontin et al. 2017), and that most TRACE loops do not show

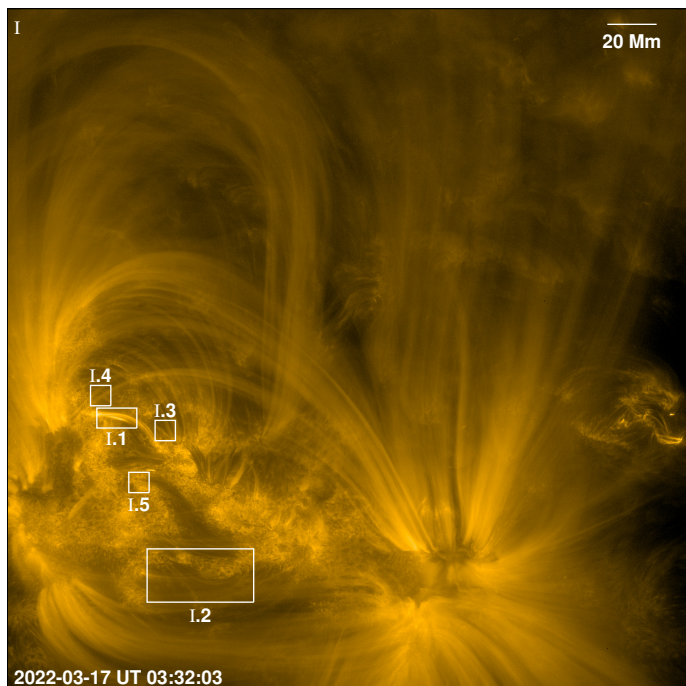


**Fig. 1.** Overview of AR12965 (AR-I) as observed with EUV/HRI<sub>EUV</sub> on 2022 March 17. The snapshot shows the full field of view of the HRI<sub>EUV</sub> covering AR-I. See Table 1 for observational details. Boxes I.1–I.5 cover different regions exhibiting intermittent heating events in the corona that we analyzed. Close-up views of regions I.1 and I.2 are displayed in Figs. 2 and 4, respectively. Regions I.3–I.5 are displayed in Fig. A.2. The intensity of the displayed image is on a log-scale. North is roughly up. See Sects. 2, 3 and the Appendix A for discussion.

evidence of magnetic braiding. Furthermore, van Ballegoijen et al. (2011) examined X-ray images of solar active region loops and found that there were only a few sites where loops appeared to cross each other. From this they concluded that braiding, if present on the Sun, should exist on smaller transverse scales, corresponding to the angular (spatial) scales of less than 5". Using EUV and X-ray observations of an active region, Parenti et al. (2010) observed relaxation and multi-thermal evolution of tangled loops in a post-flare arcade. The lack of overwhelming evidence for magnetic braiding in the X-ray observations could be due to their generally lower spatial resolutions of worse than 1". Despite resolving 1" on the Sun, TRACE observations did not reveal wide-spread coronal braiding. It could be that coronal braiding is observable on angular scales of less than 1".

To this end, using high resolution (0.4"– 0.5"), high cadence (~5 s) coronal EUV observations recorded by the High-resolution Coronal Imager sounding rocket experiment (Hi-C; Kobayashi et al. 2014), Cirtain et al. (2013) found signatures of spatially resolved magnetic braids and the associated coronal heating in two cases of low-lying loops. They implied that the observable signatures of coronal braiding would be common at small spatial scales of the order of 150 km. Magnetic field extrapolations revealed that one of the braided loops in Hi-C images is associated with a low-lying twisted flux rope (Thalmann et al. 2014), over a penumbral filament region. Those loops are not associated with the main opposite polarity patches of that active region. For the other example of small braided loops in Fig. 3 of Cirtain et al. (2013), van Ballegoijen et al. (2014) suggest that it may be due to moss regions in that active region. Because Hi-C was flown on a suborbital rocket flight, the duration of ob-

servations it could record was limited to some 5 minutes only. Despite this limitation, Hi-C set a benchmark for high-resolution and high-cadence coronal observations by revealing the highly dynamic sub-arcsec structure of the solar corona.

More recently, Antolin et al. (2021) observed signatures of nanojets and accompanying coronal heating in loops undergoing episodes of coronal rain. The authors suggest that the nanojets are produced as a result of magnetic reconnection and subsequent relaxation of braided coronal loops. Furthermore, Sukarmadji et al. (2022), who observed additional cases of nanojets in magnetic features hosting cooler plasma including coronal rain suggest that nanojets are a general result of magnetic reconnection and that not only braiding, but also Kelvin–Helmholtz and Rayleigh–Taylor instabilities can cause them. An open issue concerning nanojets is whether they occur in coronal loops that do not exhibit any signature of cool plasma or coronal rain. Therefore, there is a strong need to find more examples of braided coronal fields, especially in normal coronal loops.

Here we present evidence of magnetic braiding and the associated intermittent coronal heating in four active regions, using novel high-resolution, high-cadence observations by the 174 Å EUV High Resolution Imager (HRI<sub>EUV</sub>) of the Extreme Ultraviolet Imager (EUI; Rochus et al. 2020) onboard the Solar Orbiter mission (Müller et al. 2020). The data were obtained during the first perihelion observing campaigns of EUI (see Table 1 for details). During this period, with its full-width at half maximum (FWHM) of point spread function (PSF) equivalent to ~0.35" as seen from Earth, EUI/HRI<sub>EUV</sub> resolves the structures in the solar corona comparably as well as or better than Hi-C (Kobayashi et al. 2014; Rachmeler et al. 2019). In addition, some of the EUI observations provide not only a higher cadence but also longer time coverage.

## 2. Observations

The thermal response function of the HRI<sub>EUV</sub> instrument has its peak at temperatures of about 1 MK due to Fe IX (at 171.1 Å) and Fe X (at 174.5 Å and 177.2 Å). In this study, we employ HRI<sub>EUV</sub> data from three recent first perihelion observing campaigns covering active regions. Relevant information of the HRI<sub>EUV</sub> observing campaigns are summarized in Table 1. The PSF FWHM of HRI<sub>EUV</sub> is about two times the image scale per pixel. For the observed period, the spatial resolution of HRI<sub>EUV</sub> is thus in the range of 250–270 km on the Sun. We use the calibrated level-2 HRI<sub>EUV</sub> data from these campaigns (Mampaey et al. 2022). We removed the spacecraft jitter in the level-2 HRI<sub>EUV</sub> data using a cross-correlation technique (see the Appendix A.1 for details).

For the observing campaign on 2022 March 17 covering AR12965 (AR-I), we complement EUI/HRI<sub>EUV</sub> data with the co-temporal EUV observations from the Atmospheric Imaging Assembly (AIA; Lemen et al. 2012) on board the Solar Dynamics Observatory (SDO; Pesnell et al. 2012). In particular, we use the data from the six EUV passbands of SDO/AIA. The central wavelengths of these AIA filters, dominant ion species contributing to the emission in active regions and log<sub>10</sub>T (K) formation temperature of the ions are 94 Å (Fe X: 6.05; Fe XVIII: 6.85), 131 Å (Fe VIII: 5.6; Fe XXI: 7.05), 171 Å (Fe IX: 5.85), 193 Å (Fe XII: 6.2; Fe XXIV: 7.25), 211 Å (Fe XIV: 6.3), and 335 Å (Fe XVI: 6.45) (see O'Dwyer et al. 2010; Boerner et al. 2012). We processed the level-1 AIA data using the standard `aia_respice` and `aia_prep` procedures available in the `solarsoft` library (Freeland & Handy 1998). The AIA data have an image scale of 0.6" pixel<sup>-1</sup>. During this period, SDO/AIA was operating in a

**Table 1.** Details of observations recorded by the EUI/HRI<sub>EUV</sub> instrument on board Solar Orbiter.

Target ID	Date & start time (UT) <sup>a</sup>	Distance (AU) <sup>b</sup>	Scale (km) <sup>c</sup>	Cadence (s)	Duration (min) <sup>d</sup>	Carrington longitude <sup>e</sup>		NOAA AR number <sup>f</sup>	Overview Figure
						Orbiter (°)	Earth (°)		
I	2022-03-17 03:23:08	0.379	135	3	45	259	233	12965	Fig. 1
II	2022-03-19 10:41:20	0.356	127	5	60	238	202	12967	Fig. A.5
III & IV	2022-04-01 09:24:41	0.347	124	10	75	136	32	12975 & 12976	Fig. A.6

**Notes.** <sup>(a)</sup> Start time of observations corrected for time delay between Earth and Solar Orbiter. <sup>(b)</sup> Distance of Solar Orbiter from the Sun in astronomical units. <sup>(c)</sup> Image scale of HRI<sub>EUV</sub> in km per pixel. The spatial resolution is about twice this value. <sup>(d)</sup> Duration of the observational sequence in minutes. <sup>(e)</sup> Carrington longitude of Solar Orbiter and Earth. <sup>(f)</sup> NOAA active region number of the observed target.

special mode to support the EUI/HRI<sub>EUV</sub> campaign, in which its 131 Å, 171 Å and 193 Å passbands recorded data at a cadence of 6 s while 94 Å, 211 Å and 335 Å filters recorded data every 96 s. A snapshot of the AIA 171 Å image from this period in Fig. A.1 shows the view of AR-I from the vantage point of Earth.

This active region was also observed by the X-Ray Telescope (XRT; Golub et al. 2007) on board the Hinode mission (Kosugi et al. 2007). Here we use the data from the Al-poly and Be-thin filters of Hinode/XRT. These images are first deconvolved with the model point spread function of XRT and then processed with `xrt_prep` procedure distributed in `solarsoft`. The XRT data have an image scale of about 1'' pixel<sup>-1</sup> and a cadence of 30 s. The details on extracting features of interest in AR-I from HRI<sub>EUV</sub>, AIA, and XRT observations are provided in the Appendix A.2.

For the remaining two EUI campaigns (i.e. on 2022 March 19 and 2022 April 01; see Table 1), mainly for simplicity, we did not make use of complementary coronal SDO/AIA and or Hinode/XRT data. Nevertheless, to understand the connection between the coronal braids and the chromosphere, we did consider AIA 304 Å data that reveal cooler chromospheric and transition region structures around log<sub>10</sub>*T* (K) of 4.7 sampled by He II. These AIA 304 Å data are also processed in the same way as above (but we skipped the respire step for simplicity).

Overall, the four active regions considered in this study are representative of active regions that exhibit weak to moderate flaring activity (see the Appendix A for a related discussion). Here, the time-stamps of HRI<sub>EUV</sub> observations quoted are corrected for the time delay between Earth and Solar Orbiter<sup>1</sup>.

### 3. Braided loops in the core of an active region

Using HRI<sub>EUV</sub> observations, we detected a localized brightening in a system of coronal loops<sup>2</sup> in the core of AR-I on 2022 March 17 around UT 03:32 (see box AR-I.1 in Fig. 1). The loops themselves appear about 13 minutes after a small B-class flare in AR-I (see Fig. A.4), and thus they could be considered as post-flare loops. Upon a closer examination, we found that the localized brightening is associated with a pair of coronal loops that were entwined or braided. The braiding is most clearly seen between the locations marked E and W in Fig. 2a. Although the braiding

<sup>1</sup> Hinode is in a Sun-synchronous orbit around Earth at an altitude of about 650 km. The SDO is in an inclined geosynchronous orbit around Earth at an altitude of about 35.756×10<sup>3</sup> km. The light travel time from these telescopes to Earth is in the range of 0.002 s to 0.12 s. This is more than three orders of magnitude smaller compared to the light travel time between Solar Orbiter and Earth. Therefore, for simplicity, we consider the Earth time itself as reference to correct the timestamps of HRI<sub>EUV</sub> images.

<sup>2</sup> In this paper we refer to a well-defined arch-like EUV feature a loop. Multiple such loops then form a system of loops.

is not clear in SDO/AIA data, because of its limited spatial resolution, different AIA passbands do show local enhancement in the EUV emission at the location where EUI sees the braiding (Fig. 2b–e). The braided loops relax over the course of the next 3 minutes and give rise to coronal loops that run more parallel to each other. Simultaneously, the localized brightening also fades away (Figs. 2f and A.3). We note that only this pair of the loops that show apparent braiding exhibit localized brightening. All the other loops observed with HRI<sub>EUV</sub> that formed in the aftermath of this B-class flare show no apparent braiding signatures and exhibit rather uniform brightening along their length, unlike the event that we discussed. The localized brightening is also consistent with the small-angle reconnection scenario of braided loops and nanojets (Antolin et al. 2021).

It could be argued that this apparent braided feature is actually a line of sight superposition of emission from two non-interacting loops. For this to be the case, however, there should be two loops with intersected localized brightenings in the line of sight that fade in a similar way. This ad-hoc arrangement of non-interacting loops that exhibit coherent evolution is, however, unlikely. It could also be argued that EUV absorption due to raining cooler material could give the impression of braiding. However, we do not find any signatures of hotter loops in the direction of the initial dark feature (between points E and W in Fig. 2a). At the same time, there is no evidence of any raining blobs either at that location in AIA 304 Å passband (sensitive to cooler plasma). This supposed EUV absorption feature again requires a special arrangement of loops not supported by observations. Therefore, we suggest that the observed feature is indeed a braided system of coronal loops.

The localized brightening at the site of braiding appears coherent over length scales of 2–5 Mm. To investigate the evolution of coronal emission from distinct regions of the braided loops, we considered two pixels, marked E and W in Fig. 2a, one on each of the two braided loops in the localized brightening region. These pixels are separated by more than 2 Mm; that is about seven times the spatial resolution of HRI<sub>EUV</sub> at that time. The HRI<sub>EUV</sub> intensities from these two pixels show simultaneous increases for roughly 120 s. Thereafter, the intensity decreases monotonically, although more rapidly around W compared to that of E (red and blue light curves in Fig. 3). The appearance of braided loops together with the localized intensity increase followed by the relaxation of the loops and the decrease in the intensity is consistent with the scenario that magnetic energy stored in the coronal braids is released to heat the plasma on timescales of about 3 minutes.

The AIA EUV diagnostics of this region shed further light on the thermal evolution associated with relaxation of coronal braids, even though the internal structure cannot be resolved. As we identified in Fig. 2, the AIA EUV filters detected the local-



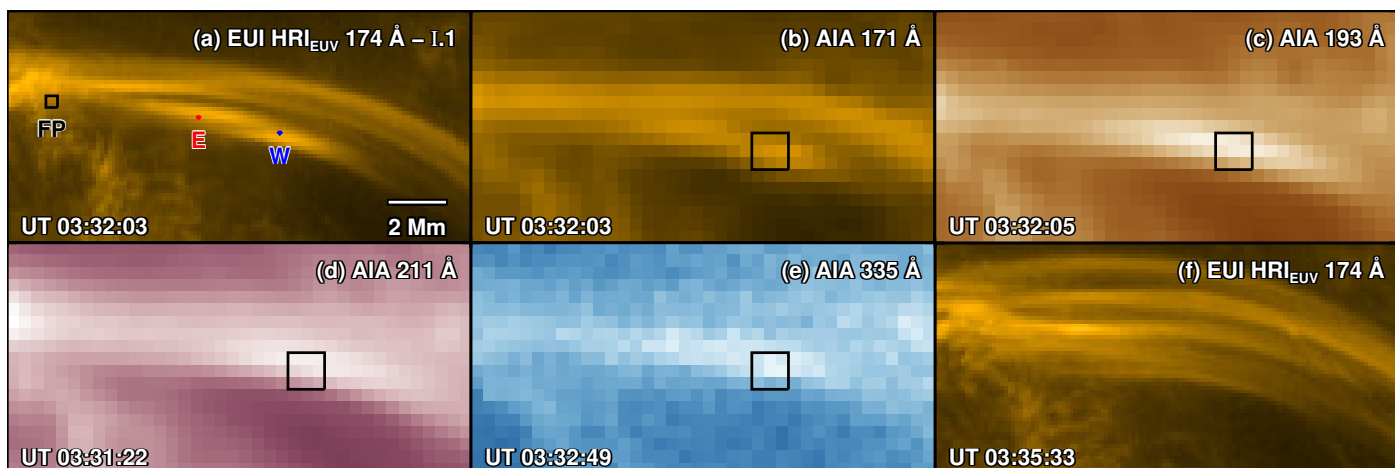


**Fig. 2.** Braided coronal loops. Panel (a) displays a segment of braided coronal loops observed in the core of AR-I with HRI<sub>EUV</sub> (box I.1 in Fig. 1). Red and blue pixels, labeled E and W, mark the eastern and western sections of the braided loops, while the black box FP is placed at the footpoint region of these loops. The time-stamp of the snapshot and the spatial scale (using a 2 Mm bar) are also indicated. Panels (b)–(e) display the same braided loops from the perspective of SDO/AIA in different EUV passbands as labeled. The projected area of these panels is roughly the same as that of panel (a). The black box in panels (b)–(e) is overlaid on the location of the braided loops. The mean emission of the respective AIA passbands computed from the region covered by this black box is plotted in Fig. 3. In panel (f), the HRI<sub>EUV</sub> snapshot shows the relaxed state of the initially braided loops, only ca. 3 minutes after panel (a), see also Fig. A.3 for the detailed evolution of the braided loops. The intensities of all the snapshots are on a square-root-scale. See Sect. 3 for a discussion. An animation of panel-a is available online.

ized brightening associated with the braided loops. We considered a region overlaid on this brightening and derived the mean intensity as a function of time in the six AIA EUV passbands, excluding the AIA 304 Å filter (black squares in Fig. 2b–e). The light curves from three of the six EUV filters are plotted in Fig. 3. The 193 Å, 211 Å and 335 Å filters have their peak thermal responses at progressively higher temperatures, i.e. at  $\log_{10}T$  (K) of 6.2, 6.3, and 6.45, respectively. Here we found that the light curves from these filters exhibit a progressively earlier rise phase with increasing temperature and all of them start rising in intensity before HRI<sub>EUV</sub>, which has a thermal response peak around  $\log_{10}T$  (K) of 6. This suggests that the localized brightening associated with heating at the site of coronal braiding is caused by multi-thermal plasma. We further quantified this multi-thermal nature of plasma using a differential emission measure analysis (discussed in the Appendix B). Such sequential signal of emission in filters sensitive to progressively cooler temperatures is thought to be a signature of plasma cooling in coronal loops (Viall & Klimchuk 2012). However, here we observed that the intensity evolution is much rapid on timescales of  $\sim 200$  s compared to the longer cooling timescales, on the order of 1000 s, as reported by Viall & Klimchuk (2012).

Furthermore, we visually identified the footpoint closer to the braiding feature. This footpoint region shows a localized intensity enhancement around 03:34 UT, following the peak in HRI<sub>EUV</sub> intensity (black curve in Fig. 3). In the vicinity of the visually identified footpoint, we also observed similar localized intensity enhancements, but shifted in time, that are likely associated with the other overlying loops. This kind of footpoint intensity enhancements could be related to the deposition of energy in the transition region from a heating event. In case where the footpoint is associated with the braided loop system, the heating event could be linked to the energy released from the relaxation of observed braids.

To conclude, we see clear evidence for the existence of braids within a system of coronal loops and for their subsequent relaxation. The timing of the emission originating at different temper-

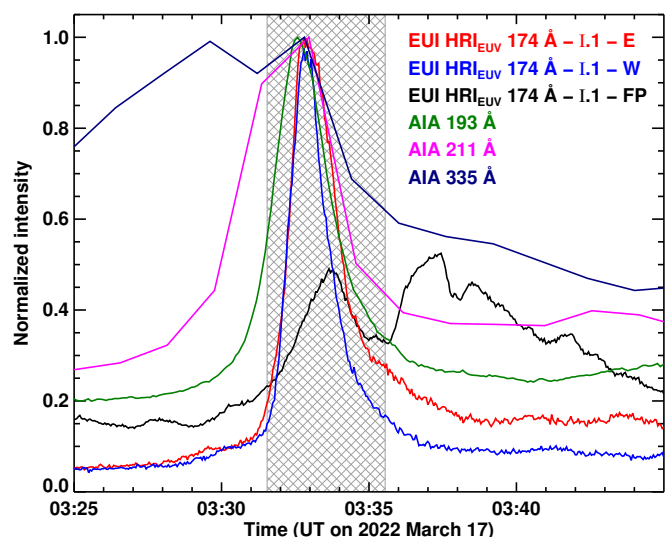


**Fig. 3.** Extreme ultraviolet emission characteristics of the braided loops. We plot the normalized EUV intensity from both the HRI<sub>EUV</sub> and SDO/AIA instruments. The red and blue light curves show the time evolution of EUV emission from braided loops at the pixels marked E and W in Fig. 2a. The black curve is the average intensity from the footpoint region of the braided loops, labeled FP, in Fig. 2a. The SDO/AIA light curves (dark green: 193 Å; magenta: 211 Å; dark blue: 335 Å) show the mean EUV intensity computed from the black boxes overlaid on the braided loops in the respective passband panels in Fig. 2. The hatched region spans the duration covered by Fig. A.3, which shows the relaxation of braided loops. See Sect. 3 for a discussion.

atures indicates a rapid heating and multi-thermal evolution of the plasma in the loop in response to the relaxation of the braids.

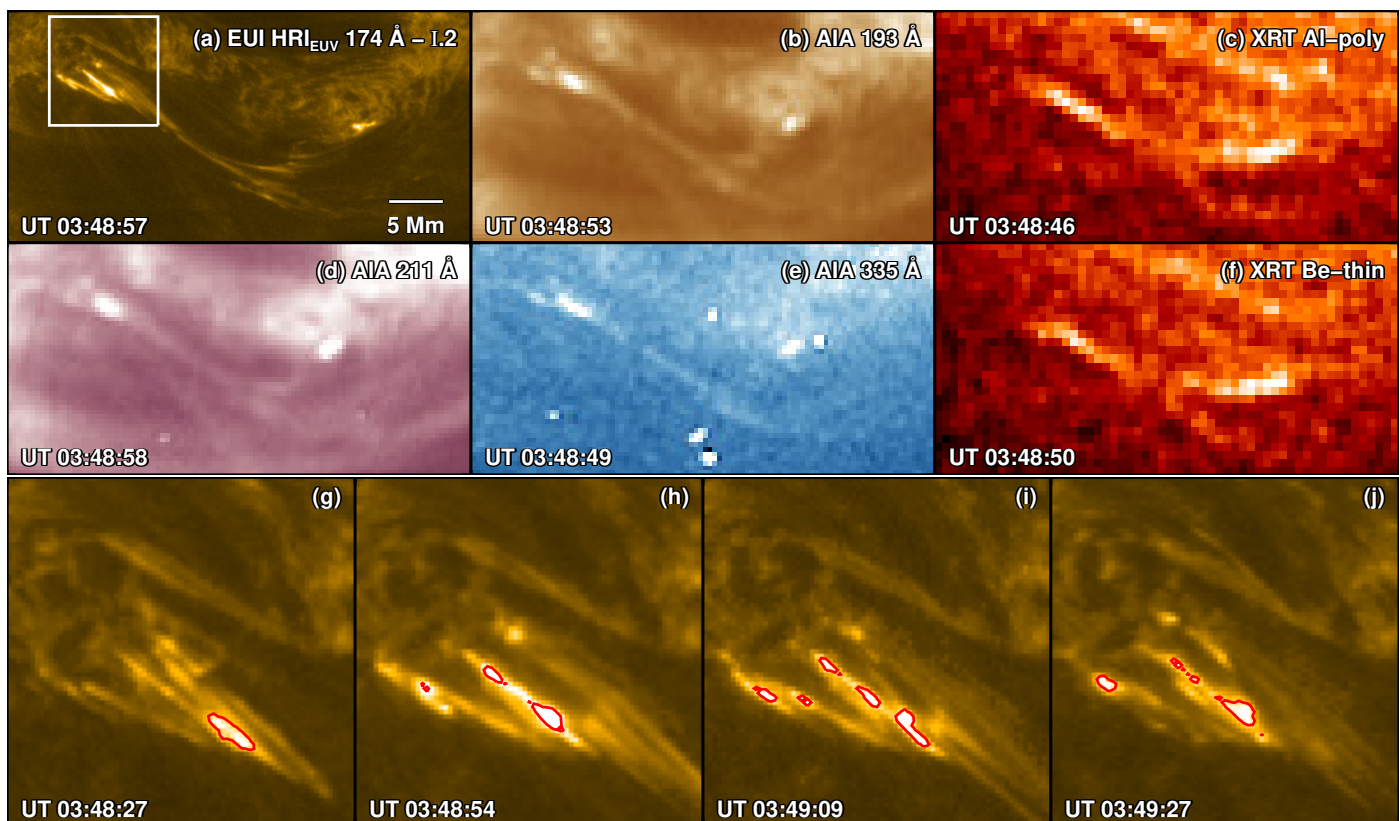


**Fig. 4.** Untangling of braided loops and coronal heating over filamentary structures. Panel (a) is a HRI<sub>EUV</sub> snapshot that captures coronal loops with complex braided structuring over cooler filaments in the southern portion of the core of AR-I (see box AR-I.2 in Fig. 1). The white box outlines the footpoint regions of the loops. Panels (b), (d), and (e) are snapshots covering roughly the same region as in panel (a), but with EUV passbands of SDO/AIA as indicated. Panels (c) and (f) are near-simultaneous snapshots from a pair of soft X-ray channels of Hinode/XRT. Panels (g)–(j) are zoomed-in view of the footpoint regions of the loops as seen with HRI<sub>EUV</sub> (white box in panel-a). The red contours outline apparent blob-like features observed near the footpoints of the braided loops. The contours enclose regions that exceed certain intensity threshold in each snapshot and are overlaid to mainly guide the eye. All the snapshots are displayed on a square-root-scale. See Sect. 4 for a discussion. Animations of panel-a and panel-g are available online.

#### 4. Rapidly evolving braided loops and coronal heating over filamentary structures

While the example of braiding presented in Fig. 2 is associated with conventional coronal loops in the core of an active region, we also identified other braiding-related coronal heating events in AR-I, that originate over chromospheric filamentary structures that appear darker in EUV due to absorption. In Fig. 4, we present such an example of intermittent coronal heating during the untangling of loops over filamentary structures (see box AR-I.2 in Fig. 1). Unlike the more gentle untangling observed in conventional loops (Fig. 2), the loops over filaments presented in Fig. 4a untangle more impulsively. Here both SDO/AIA and Hinode/XRT instruments detected coronal emission (Fig. 4b–f), during the untangling of the loops that was clearly seen in HRI<sub>EUV</sub> images (see the animation associated with Fig. 4a). Furthermore, nanojet features similar to those discovered by Antolin et al. (2021) are also apparent in this case in the HRI<sub>EUV</sub> images. In addition, footpoint brightenings similar to rapid moss variability seen in active region cores associated with 5–7 MK hot loops (e.g. Testa et al. 2014; Chitta et al. 2018), are also observed. The soft X-ray emission as observed by Hinode/XRT is organized in a more loop-like feature whereas the HRI<sub>EUV</sub> images of the same structure show substantial complexity in both space and time.

This spatial and temporal complexity extends also to the footpoints of these untangling loops (white box in Fig. 4a and

Fig. 4g–j). Here the EUV emission is organized into distinct blob-like features that exhibit back and forth motions including signatures of splitting and merging (red-contoured regions in Fig. 4g–j). These dynamics could be closely related to the small-angle reconnection scenario of nanojets (Antolin et al. 2021). This suggests that the energy deposition at the footpoints is quite bursty and is spatially less coherent than in the braids in conventional loops displayed in Fig. 2.

We observed a similar heating event associated with braided loops over filamentary features on 2022 March 19. In the decaying AR12967 (AR-II; see Fig. A.5), we detected a system of roughly 10–15 Mm long, compact coronal loops that exhibited rapid evolution including clear signs of braiding (see Fig. 5). In this particular example, we also observed the ejection of confined plasma jets from one end of the loop system.

As demonstrated in Fig. 5a–i, this compact loop system as a whole shows intensity variation over a period of about 180 s. But we observed that individual loops within the system evolve much more rapidly. The system first appears as a single bright loop in the early stages (Fig. 5a). Subsequently, multiple bright loops appear and these spread about 1–2 Mm across the length of the loop. Not only are these loops apparently braided, but the whole system evolves from a nearly untangled state (as seen in EUV images; which does not preclude pre-existing tangling in cooler plasma structures in that system), to a highly braided

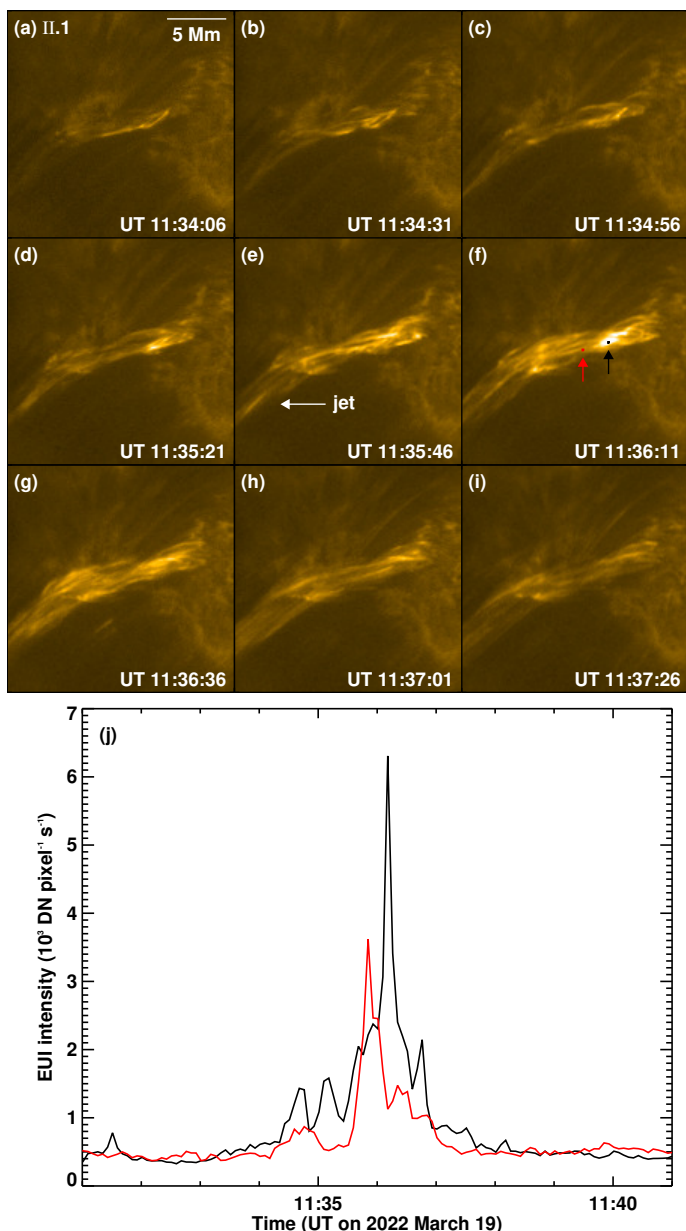


**Fig. 5.** Rapidly evolving braids in a compact loop system. Panels (a)–(i) capture the formation and evolution of braided coronal loops in the decaying AR-II (white box in Fig. A.5). In panel (e) the arrow points to a plasma jet. In panel (f) the red and black arrows point to a pair of pixels placed along the braided loops. The red and black HRI<sub>EUV</sub> light curves plotted in panel (j) are obtained from the corresponding colored pixels in panel (f). The intensity of the displayed images is on a square-root-scale. See Sect. 4 for a discussion. Animation of panel-a is available online.

state on short timescales of 60 s (e.g. compare development of braided structures from panels a to c to e of Fig. 5). This is evident in morphological changes to the structures in subsequent panels that are temporally separated by only 25 s. But the very appearance of apparent tangling in the EUV suggests that energy stored in the pre-existing tangling is being dissipated to heat the plasma (see further discussion on visibility of braids in Sect. 6).

Similar to Fig. 4, this particular braided system also shows more spatial complexity and smaller-scale structuring compared to the loops presented in Fig. 2. In contrast to the near-

simultaneous evolution of HRI<sub>EUV</sub> intensity from regions separated by about 2 Mm along the loops in Fig. 2 (see Fig. 3), two regions from the compact loops with similar separation exhibit distinct intensity variations on shorter timescales (see Figs. 5f and 5j)<sup>3</sup>. This points to a more spatially and temporally sporadic release of magnetic energy in these compact braided loops.

Additional examples of coronal braids over chromospheric filamentary structures are presented in the Appendix A.3.

## 5. Timescales associated with intermittent heating events

The 3 s high-cadence HRI<sub>EUV</sub> data from 2022 March 17 allow us to probe the timescales associated with the thermal response to magnetic reconnection in braiding events. For this we compare the case of the braiding within the coronal part of a loop (discussed in Sect. 3) and the events of the type found over the filamentary structures (Sect. 4).

These two types of events show a clear distinction in their variability. As shown in Fig. 3, at the location of localized brightening associated with coronal braids in the conventional loop system, the HRI<sub>EUV</sub> light curves exhibit a smooth rise and fall of intensity over a period of 4–5 minutes without a clear temporal substructure. But the coronal loops over filaments displayed in Fig. 4 demonstrate burstiness during untangling, which might be a signature of shorter term variability in thermal response of plasma to intermittent heating.

To understand this effect, we hand-picked a few more intermittent heating events from the core of AR-I that has been observed at the highest cadence. Snapshots of these events are displayed in Fig. A.2 and their spatial relation to the active region core is identified with the respective numbered boxes in Fig. 1. The events AR-I.3 and AR-I.4 are associated with loops while the event AR-I.5 is a rapid moss variability feature at the footpoints of hotter loops. The light curves from these regions in comparison to the light curve from point-E of conventional braided loops in Fig. 2a are shown in Fig. 6. It is evident that these intermittent heating events AR-I.3–AR-I.5 exhibit temporal variability of emission on much shorter timescales of 10–30 s compared to that of the braided loops in Fig. 2a. Such shorter-term variability of EUV emission on timescales less than 60 s is also observed in the compact loop system displayed in Fig. 5j. Furthermore, considering the footpoint response alone, the moss variability (i.e. light curve of event AR-I.5 in Fig. 6) is more rapid than that observed at the footpoints of the braided loops in Fig. 2a (i.e. the black curve in Fig. 3). These findings suggest that intermittent energy release in the corona through reconnection could have a range of temporal scales from a few 10s to a few 100 s or even longer. The differences in timescales could also be due to the fact that the braided loops in Fig. 2 appear in the aftermath of a B-class flare. The flare itself could correspond to a very different initial magnetic topology, involving many processes, which could in-turn govern the relatively longer timescales of the relaxation of braid that followed. The data also suggest that the temporal variability can be related to the degree of spatial coherence of energy deposition in the corona, i.e. the more temporally intermittent events appear more patchy or

<sup>3</sup> Each of the remaining eight pixels surrounding the respective red and black pixels along the braided loops in Fig. 5 show nearly similar and temporally coherent intensity variations on shorter timescales. This suggests that these intensity variations on shorter timescales that we observed are indeed of the solar origin.



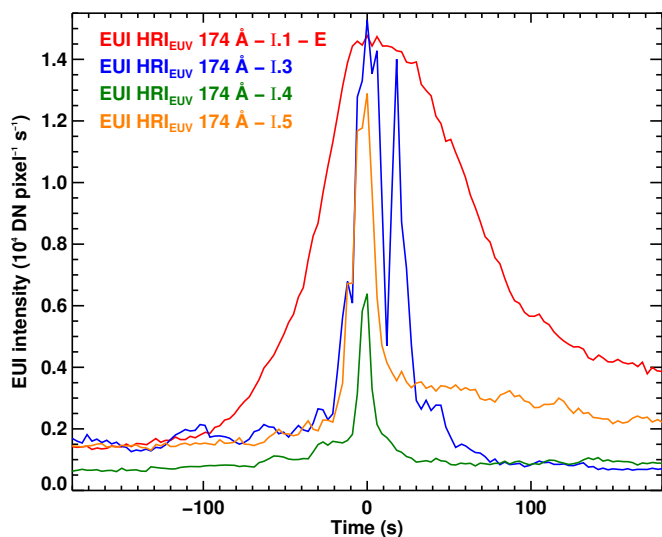


**Fig. 6.** Comparison of  $\text{HRI}_{\text{EUV}}$  light curves from different heating events. The curve in red is same as that in Fig. 3 (i.e. from point-E of the braided loop system in Fig. 2), but not normalized to its peak value. The other three light curves (i.e. I.3–I.5) are obtained from center of the respective panels in Fig. A.2. The 0 s mark along the abscissa (i.e. the time-axis) is with respect to the peak of each of the light curves. See Sect. 5 for a discussion.

bursty in space. However, this would have to be quantified in a future study.

## 6. Discussion

One of the most influential cartoons in solar coronal physics is that of braided loops, as proposed by Parker (1972, 1983). The appearance of the observed compact braided loop system in Fig. 5 is reminiscent of this cartoon scenario. Could a rapidly evolving braiding feature like this be used as a test-case to understand how such structures might be generated in the corona? To address this question we further discuss the evolution of this loop system.

As described in Sect. 4, this particular compact loop system develops tangling on timescales of about 25 s. Assume that each bright loop within the system is connected to a pair of isolated magnetic field patches at both footpoints in the photosphere. The magnetic field patches in the photosphere move with typical speeds of about  $1 \text{ km s}^{-1}$  (e.g. Chitta et al. 2012). Then it would take on the order of 1000 s for a pair of initially parallel loops to exhibit apparent criss-cross pattern within a system that is 1–2 Mm across. Parker (1988) predicts that for a 10 Mm-long loop system (comparable to the observed compact loop system in Fig. 5), a steady state of energy injection from slow footpoint motions against the release of magnetic energy through reconnection in the tangled coronal magnetic fields, is reached in about 5000 s. But the observed braided features in the compact loops (Fig. 5) develop and evolve on a much shorter timescale of about 25 s. This indicates that footpoint motions alone would be too slow to directly explain the development of rapid braiding in this system. It is then likely that additional magnetic disturbances, such as the emergence and cancellation of surface magnetic flux, and the associated energy built-up and release through reconnection (Priest et al. 2018; Chitta et al. 2020), could be necessary to explain the rapidly evolving system of braided loops. In this context, Tiwari et al. (2014) observed that the coronal

brightenings in the Hi-C braided loops (Cirtain et al. 2013) were externally triggered by photospheric flux cancellation.

Another important point to consider here is that the loops in Fig. 5 already become visible in the EUV passband sensitive to emission from 1 MK, while the tangling is apparently still developing. This means that the dissipation of energy that is responsible for plasma heating in this system is already in progress. This is possible when part of the pre-existing tangling begins to relax through reconnection to heat the plasma. The brightening of loops that are already tangled to begin with could also then give the impression of rapid development of braiding. In this regard, in all the discussed cases, coronal braids become apparent only for a limited amount of time when the magnetic field is relaxing. This does not, however, preclude the existence or buildup of magnetic tangling in the corona as proposed by Parker (1988). It only means that the (presumably) slow buildup of magnetic tangling in the corona on timescales of several 1000 s, in itself, is not observed, at least in the passband used. The tangling could develop at different temperatures. While the tangling may buildup slowly in the corona, the braids become apparent in remote-sensing observations only when a part of the tangled magnetic field is already relaxed to heat the plasma such that the emission from that heated plasma is captured by a filter (with a given thermal response). However, 3D MHD models predict that an efficient dissipation of currents may prevent magnetic fields from reaching a highly tangled state in the corona (Peter et al. 2022). Such 3D MHD models, in general, are limited by the very high diffusivity and by design, do not allow for the build-up of strong current sheets. Moreover, spatial and temporal information on the onset of reconnection that relaxes braids in real coronal loops, subjected to slow stressing, is unknown.

In this context, except for the braided conventional loop system presented in Fig. 2, we did not find clear or unambiguous signatures of widespread braiding in longer coronal loops connecting the main opposite polarity patches of active regions. This could be due to the sensitivity of  $\text{HRI}_{\text{EUV}}$  to emission from 1 MK plasma, implying that the braids could be more apparent in emission from plasma at higher temperatures. But as pointed out by van Ballegoijen et al. (2011), even the X-ray diagnostics that sample emission from higher temperature plasma do not reveal widespread braiding signatures, albeit at much lower spatial resolution. When the coronal magnetic fields are subjected to continual stressing from slow footpoint motions, the question of why only a few loop systems like the one presented in Fig. 2 exhibit observable braided structures even down to temperatures of 1 MK, while most of the longer loops do not, needs further investigation using numerical simulations.

The other coronal braiding examples that we presented here are observed over low-lying chromospheric filamentary structures (see additional discussion in Appendix C). The two braiding examples that Cirtain et al. (2013) discussed also fall into this category. This suggests that chromospheric filaments might play a role in the observability of coronal braids down to temperatures of 1 MK.

Earlier studies using Hi-C imply that observable signatures of braiding would be common at small spatial scales of the order of 150 km (Cirtain et al. 2013). The new EUV observations used here with a spatial resolution of about 250–270 km, comparable to or better than Hi-C, show that signatures of braiding are not common at such small scales. This could be either because the braiding is happening on even smaller scales than previously thought, or it simply eludes observations for the reasons outlined above, or is not widespread at all. To this end, the two future missions, Solar-C EUV High-Throughput Spectroscopic

Telescope (Shimizu et al. 2019) and the Multi-slit Solar Explorer (De Pontieu et al. 2022), could shed light on the multi-thermal observability of braided coronal loops.

## 7. Conclusion

Using novel high-resolution and high-cadence EUV/HRI<sub>EUV</sub> observations, we present signatures of intermittent coronal heating during the untangling of braided loops. Our observations suggest that apparent tangling and subsequent relaxation of braided loops is perhaps more common or observable over chromospheric filamentary structures, although the statistics are as yet poor. For one example of a conventional coronal loop system, we show that the braiding evolves on timescales of minutes and remains observable down to temperatures of 1 MK. The localized brightening caused by heating at the site of braiding appears spatially more coherent (Fig. 2). This suggests that a more gentle mode of reconnection might be operating at the location of this coronal braiding. In comparison, more variable and impulsive reconnection might be operating in the braided loops overlying cooler filamentary structure (Figs. 4, 5, A.7, A.8). In these cases, energy release is likely at smaller spatial scales, which then leads to the formation of blob-like features and rapidly evolving EUV emission from those loops. All these features are also consistent with the interpretation of the recently discovered nanojets (Antolin et al. 2021; Sukarmadji et al. 2022). While providing evidence for intermittent coronal heating from the relaxation of braided loops, our study identifies the operation of both gentle and impulsive modes of energy release through reconnection in the solar corona.

*Acknowledgements.* The authors thank the anonymous referee for constructive comments that helped improve the manuscript. L.P.C. thanks Patrick Antolin, Northumbria University, for insightful discussions on nanojets. L.P.C. gratefully acknowledges funding by the European Union. Views and opinions expressed are however those of the author(s) only and do not necessarily reflect those of the European Union or the European Research Council (grant agreement No 101039844). Neither the European Union nor the granting authority can be held responsible for them. S.P. acknowledges the funding by CNES through the MEDOC data and operations center. D.M.L. is grateful to the Science Technology and Facilities Council for the award of an Ernest Rutherford Fellowship (ST/R003246/1). The ROB team thanks the Belgian Federal Science Policy Office (BELSPO) for the provision of financial support in the framework of the PRODEX Programme of the European Space Agency (ESA) under contract numbers 4000134474 and 4000136424. W.L. and M.C.M.C. acknowledge support from NASA's SDO/AIA contract (NNG04EA00C) to LM-SAL. Solar Orbiter is a space mission of international collaboration between ESA and NASA, operated by ESA. The EUV instrument was built by CSL, IAS, MPS, MSSL/UCL, PMOD/WRC, ROB, LCF/IO with funding from the Belgian Federal Science Policy Office (BELSPO/PRODEX PEA 4000134088); the Centre National d'Etudes Spatiales (CNES); the UK Space Agency (UKSA); the Bundesministerium für Wirtschaft und Energie (BMWi) through the Deutsches Zentrum für Luft- und Raumfahrt (DLR); and the Swiss Space Office (SSO). AIA is an instrument on board the Solar Dynamics Observatory, a mission for NASA's Living With a Star program. Hinode is a Japanese mission developed and launched by ISAS/JAXA, collaborating with NAOJ as a domestic partner, NASA and STFC (UK) as international partners. Scientific operation of the Hinode mission is conducted by the Hinode science team organized at ISAS/JAXA. This team mainly consists of scientists from institutes in the partner countries. Support for the post-launch operation is provided by JAXA and NAOJ(Japan), STFC (U.K.), NASA, ESA, and NSC (Norway). We are grateful to GOES team for making the data publicly available. This research has made use of NASA's Astrophysics Data System.

## References

Antolin, P., Pagano, P., Testa, P., Petralia, A., & Reale, F. 2021, *Nature Astronomy*, 5, 54  
 Asgari-Targhi, M., van Ballegooijen, A. A., & Davey, A. R. 2019, *ApJ*, 881, 107  
 Boerner, P., Edwards, C., Lemen, J., et al. 2012, *Sol. Phys.*, 275, 41

Breu, C., Peter, H., Cameron, R., et al. 2022, *A&A*, 658, A45  
 Chitta, L. P., Peter, H., Priest, E. R., & Solanki, S. K. 2020, *A&A*, 644, A130  
 Chitta, L. P., Peter, H., & Solanki, S. K. 2018, *A&A*, 615, L9  
 Chitta, L. P., van Ballegooijen, A. A., Rouppe van der Voort, L., DeLuca, E. E., & Kariyappa, R. 2012, *ApJ*, 752, 48  
 Cirtain, J. W., Golub, L., Winebarger, A. R., et al. 2013, *Nature*, 493, 501  
 De Pontieu, B., Testa, P., Martínez-Sykora, J., et al. 2022, *ApJ*, 926, 52  
 Freeland, S. L. & Handy, B. N. 1998, *Sol. Phys.*, 182, 497  
 Golub, L., DeLuca, E., Austin, G., et al. 2007, *Sol. Phys.*, 243, 63  
 Gudiksen, B. V. & Nordlund, Å. 2002, *ApJ*, 572, L113  
 Hannah, I. G. & Kontar, E. P. 2012, *A&A*, 539, A146  
 Klimchuk, J. A. 2006, *Sol. Phys.*, 234, 41  
 Kobayashi, K., Cirtain, J., Winebarger, A. R., et al. 2014, *Sol. Phys.*, 289, 4393  
 Kosugi, T., Matsuzaki, K., Sakao, T., et al. 2007, *Sol. Phys.*, 243, 3  
 Lemen, J. R., Title, A. M., Akin, D. J., et al. 2012, *Sol. Phys.*, 275, 17  
 Mampaey, B., Verbeeck, F., Stegen, K., et al. 2022, *Solo/EUI Data Release 5.0 2022-04*, <https://doi.org/10.24414/2qfw-tr95>, published by Royal Observatory of Belgium (ROB)  
 McIntosh, S. W., de Pontieu, B., Carlsson, M., et al. 2011, *Nature*, 475, 477  
 Müller, D., St. Cyr, O. C., Zouganelis, I., et al. 2020, *A&A*, 642, A1  
 O'Dwyer, B., Del Zanna, G., Mason, H. E., Weber, M. A., & Tripathi, D. 2010, *A&A*, 521, A21  
 Parenti, S., Reale, F., & Reeves, K. K. 2010, *A&A*, 517, A41  
 Parker, E. N. 1972, *ApJ*, 174, 499  
 Parker, E. N. 1983, *ApJ*, 264, 642  
 Parker, E. N. 1988, *ApJ*, 330, 474  
 Pesnell, W. D., Thompson, B. J., & Chamberlin, P. C. 2012, *Sol. Phys.*, 275, 3  
 Peter, H., Chitta, L. P., Chen, F., et al. 2022, *ApJ*, 933, 153  
 Pontin, D. I., Janvier, M., Tiwari, S. K., et al. 2017, *ApJ*, 837, 108  
 Priest, E. R., Chitta, L. P., & Syntelis, P. 2018, *ApJ*, 862, L24  
 Rachmeler, L. A., Winebarger, A. R., Savage, S. L., et al. 2019, *Sol. Phys.*, 294, 174  
 Rochus, P., Auchère, F., Berghmans, D., et al. 2020, *A&A*, 642, A8  
 Schrijver, C. J., Title, A. M., Berger, T. E., et al. 1999, *Sol. Phys.*, 187, 261  
 Shimizu, T., Imada, S., Kawate, T., et al. 2019, in *Society of Photo-Optical Instrumentation Engineers (SPIE) Conference Series*, Vol. 11118, UV, X-Ray, and Gamma-Ray Space Instrumentation for Astronomy XXI, 1111807  
 Sukarmadji, A. R. C., Antolin, P., & McLaughlin, J. A. 2022, *ApJ*, 934, 190  
 Testa, P., De Pontieu, B., Allred, J., et al. 2014, *Science*, 346, 1255724  
 Thalmann, J. K., Tiwari, S. K., & Wiegmann, T. 2014, *ApJ*, 780, 102  
 Thompson, W. T. 2006, *A&A*, 449, 791  
 Tiwari, S. K., Alexander, C. E., Winebarger, A. R., & Moore, R. L. 2014, *ApJ*, 795, L24  
 van Ballegooijen, A. A., Asgari-Targhi, M., & Berger, M. A. 2014, *ApJ*, 787, 87  
 van Ballegooijen, A. A., Asgari-Targhi, M., Cranmer, S. R., & DeLuca, E. E. 2011, *ApJ*, 736, 3  
 Van Doorselaere, T., Srivastava, A. K., Antolin, P., et al. 2020, *Space Sci. Rev.*, 216, 140  
 Viall, N. M. & Klimchuk, J. A. 2012, *ApJ*, 753, 35  
 Warnecke, J. & Peter, H. 2019, *A&A*, 624, L12



## Appendix A: Observational overview

As mentioned in the main text, in this study we considered three EUV/HRI<sub>EUV</sub> observing campaigns, covering four active regions, (details given in Table 1). At the time of the HRI<sub>EUV</sub> campaign on 2022 March 17 (Fig. 1), the evolved active region AR-I was relatively quiescent. Overall, the disk-integrated soft X-ray flux in the 1–8 Å band of the Geostationary Operational Environmental Satellite (GOES) remained below C-class-flare level. Some 5 minutes before the start of this HRI<sub>EUV</sub> campaign, however, GOES detected enhancement of the soft X-ray flux due to a small B-class flare in the active region under investigation (see Fig. A.4). The decaying active region AR-II (Fig. A.5) was quiescent with no flaring activity during the time of observations on 2022 March 19. As such, the GOES soft X-ray flux level was lower than that of a C-class flare. The HRI<sub>EUV</sub> captured two active regions (AR12975: AR-III and AR12976: AR-IV) on 2022 April 1 (see Fig. A.6). During that entire day, the Sun was moderately active and produced several C-class flares from multiple active regions. The GOES soft X-ray background flux was at C level. Some of these flares could be traced to AR-III and AR-IV themselves. During the span of HRI<sub>EUV</sub> observations, however, AR-III was noticeably more active than AR-IV. In summary, our sample of three observing campaigns cover active regions from little to moderate flaring activity.

### Appendix A.1: Aligning HRI<sub>EUV</sub> image sequences

The HRI<sub>EUV</sub> observing sequences suffer from jitter. We removed this jitter by a cross-correlation technique. To this end, we first divided a given HRI<sub>EUV</sub> observing sequence into shorter sequences or overlapping chunks such that the last image of a given shorter sequence is the same as the first image of the following shorter sequence. Using a cross-correlation technique we then co-aligned all images in a given chunk to the first image in that particular shorter sequence. Because as these chunks overlap, this will result in the alignment of a given observing sequence as a whole to the first image of that sequence.

### Appendix A.2: Co-aligning HRI<sub>EUV</sub>, AIA and XRT observations

During 2022 March 17, the separation angle of Solar Orbiter with Earth was about 27°. Accordingly, the perspective of AR-I from the vantage points of Earth and Solar Orbiter were different (see Figs. A.1 and 1). To retain the high spatial resolution aspect of the HRI<sub>EUV</sub> data, here we fix the first image from 2022 March 17 sequence as the reference image. To co-align the AIA data to HRI<sub>EUV</sub> images, we first identify the AIA 171 Å image that is nearest in time to the reference image. Then the AIA data are co-registered and tracked to this nearest-in-time AIA 171 Å to remove the solar rotation. We then convert the Carrington coordinates of HRI<sub>EUV</sub> reference image to pixel coordinates in the nearest-in-time AIA 171 Å image. Then the AIA 171 Å image is re-projected by interpolation on to that pixel coordinates. In principle, this re-projected patch would correspond to the HRI<sub>EUV</sub> field of view as observed from the vantage point of the Solar Orbiter. Because of pointing uncertainties of Solar Orbiter, however, there will be some offsets between the HRI<sub>EUV</sub> reference image and the nearest-in-time re-projected AIA 171 Å image. To obtain these offsets, we cross-correlated the reference and re-projected images to obtain the more closest field of view of HRI<sub>EUV</sub> on AIA 171 Å image. This offset-corrected field of view

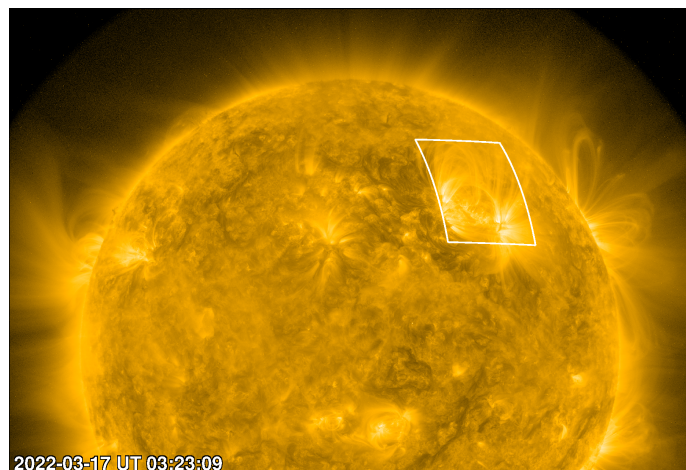


**Fig. A.1.** Solar corona as observed from the vantage point of Earth with SDO/AIA 171 Å EUV filter on 2022 March 17. The white box is the field of view of EUV/HRI<sub>EUV</sub>, covering AR-I. The displayed snapshot is closest in time with respect to the first image from the time sequence of HRI<sub>EUV</sub>. During this period, SDO/AIA was operating a special mode, which is why the roughly lower quarter of the image is not available. The intensity of the displayed image is on a log-scale. North is up. See Sect. 2 and the Appendix A.2 for details.

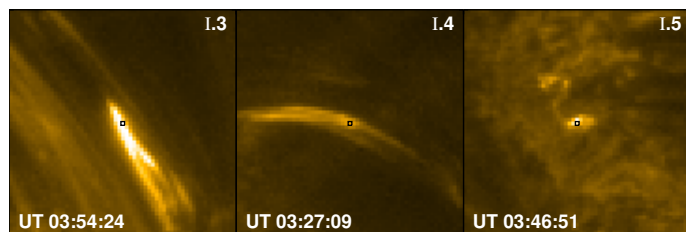


**Fig. A.2.** Intermittent heating events. Regions I.3–I.5 are outlined in Fig. 1. The light curves, I.3–I.5, in Fig. 6 are obtained from the one-pixel-wide black boxes at the center of each panel. The intensity of the displayed images is on a square-root-scale. See Sect. 5 for a discussion.

of HRI<sub>EUV</sub> is overlaid on the AIA 171 Å image in Fig. A.1. For the re-projection we made use of the World Coordinate System (WCS) package available in the solarsoft (see Thompson 2006). With the offset-corrected pixel coordinates we re-projected the time sequence of AIA 171 Å images. Using this re-projected time sequence, we identified our regions of interest from HRI<sub>EUV</sub> images (Figs. 2 and 4) in the AIA data.

Because of the separation angle of about 27° of Solar Orbiter with Earth, the AIA data would have to be stretched and distorted by interpolation when reprojected to the HRI<sub>EUV</sub> perspective. This may introduce artefacts in the data. To avoid this, however, once identified in the reprojected AIA data, the field of view covering the regions of interest are extracted from the un-reprojected AIA data themselves (i.e. AIA data that are not reprojected to the HRI<sub>EUV</sub> perspective). This is done by visually inspecting the correspondence of the regions in both the reprojected and un-reprojected data. Once the regions are identified in the AIA data, it is straightforward to extract corresponding patches from the XRT images as well.

### Appendix A.3: Additional examples of small-scale magnetic braids

Similar to the braiding examples associated with filamentary structures discussed in the main text (Figs. 4 and 5), in Figs. A.7 and A.8, we display additional examples from the HRI<sub>EUV</sub> data of 2022 April 01. The fields of view covered by these regions are marked in Fig. A.6. In Fig. A.7, we show the rapid development of a braided loop system over a filament in the moderately active AR-III. This loop system shows substantial spatial complexity and evolves on timescales of 30 s. The morphology of this example closely resembles a braiding case presented in Fig. 3 of Cirtain et al. (2013).

Similarly, the example in Fig. A.8 overlies a penumbral region in the leading sunspot of AR12976. At this location, we observed a number of coronal loops brightening intermittently. One such event is displayed in Fig. A.8. Here a pair of coronal loops are apparently braided and the morphology of the loop system is shown to evolve on timescales of 20 s.

### Appendix B: Differential emission measure analysis

We further quantified the thermal evolution of the braided loop described in Fig. 2 (i.e., AR-I.1), using a differential emission measure (DEM) analysis by employing the aforementioned mean intensities from the six AIA EUV filters (excluding the AIA 304 Å filter). To this end, we used a regularized inversion technique (Hannah & Kontar 2012) to compute the DEM over the temperature range of  $\log_{10}T$  (K) 5.5–6.7 at two arbitrary time-steps or phases in the evolution of localized brightening: one at the time close to the peak of the AIA 193 Å intensity (referred to as peak phase) and the other at the initial rise phase (these timestamps are labeled in Fig. B.1). As an input to the inversion scheme, we provided the time-dependent AIA response functions that are calculated by setting the keywords `chiantifix`, `evenorm`, and `noblend` to 1. The AIA EUV uncertainties in intensities are calculated using the `aia_bp_estimate_error` procedure available in IDL/solarsoft. Furthermore, we set the regularization tweak parameter to 1, and the regularization multiplying factor set to 1.5. We did not use any initial guess solution. In addition, to aid the method to arrive at a positive solution, the AIA uncertainties are multiplied by a factor 1.2.

The DEMs from these rise and peak phases are plotted as a function of temperature in Fig. B.1. The DEM at the rise phase (gray curve) shows multiple local peaks with the global peak around  $\log_{10}T$  (K) of 6.4. The DEM curve flattens toward higher temperatures. In comparison, the DEM at the peak phase (black curve) shows the global peak at a lower temperature of  $\log_{10}T$  (K) of 6.2. Toward higher temperatures, this DEM shows a plateau of lower-emission around  $\log_{10}T$  (K) of 6.4 and then a steep fall toward  $\log_{10}T$  (K) of 6.6. In addition, the rise phase DEM shows significantly lower contribution from lower temperatures  $\log_{10}T$  (K) of 5.7 in comparison with the peak-phase DEM. The emission measure (i.e. the integral of DEM) is larger for the peak-phase than for the rise-phase. The overall DEM profiles from these two phases support our interpretation that the localized brightening is associated with multi-thermal plasma.

### Appendix C: Connection to the chromospheric filamentary structures

We assess that coronal magnetic braids or at least their observability is more common when they are associated with chromo-

spheric filaments. In our study, four out of five examples clearly overlie cooler filamentary structures (c.f. Figs. 4, 5, A.7, A.8). To further demonstrate the connection, we made use of the AIA 304 Å images covering these regions, some minutes before the corresponding HRI<sub>EUV</sub> observations (Fig. C.1). The regions outlined by ellipses are the locations where in HRI<sub>EUV</sub> we observed signatures of relaxing braided loops. In all these cases, the AIA 304 Å images show cooler filamentary material at the locations of HRI<sub>EUV</sub> features. Although not included, the AIA 304 Å of these features show that the filamentary material exhibits intermittent brightening similar to the HRI<sub>EUV</sub> intensity evolution.

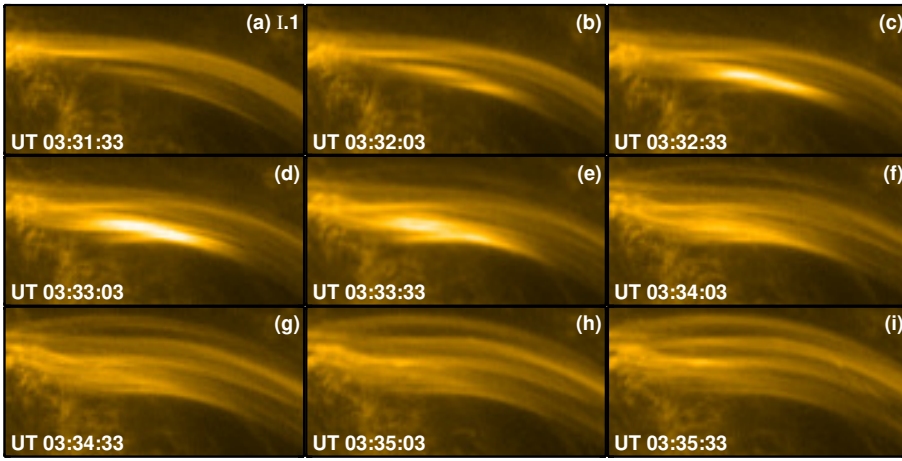


**Fig. A.3.** Image sequence showing the evolution of braided loops in Fig. 2. Subsequent panels are 30 s apart and the sequence reveals the relaxation of braided coronal loops from apparently braided to an unbraided state. Intensity of the displayed images is on a square-root-scale. See Sect. 3 for a discussion.

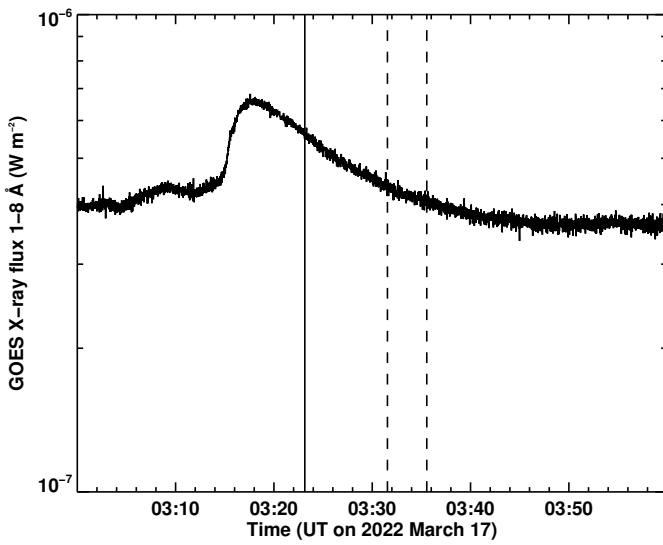


**Fig. A.4.** Soft X-ray flux. The time series shows the disk-integrated soft X-ray flux detected by the 1-8 Å band of GOES on 2022 March 17 between UT 03:00 and UT 04:00. The vertical solid line marks the start time of EUV observations (corrected for the time delay between Earth and Solar Orbiter; see Table 1 for details). The vertical dashed lines mark the duration covered by the panels in Fig. A.3. See the Appendix A for a discussion.

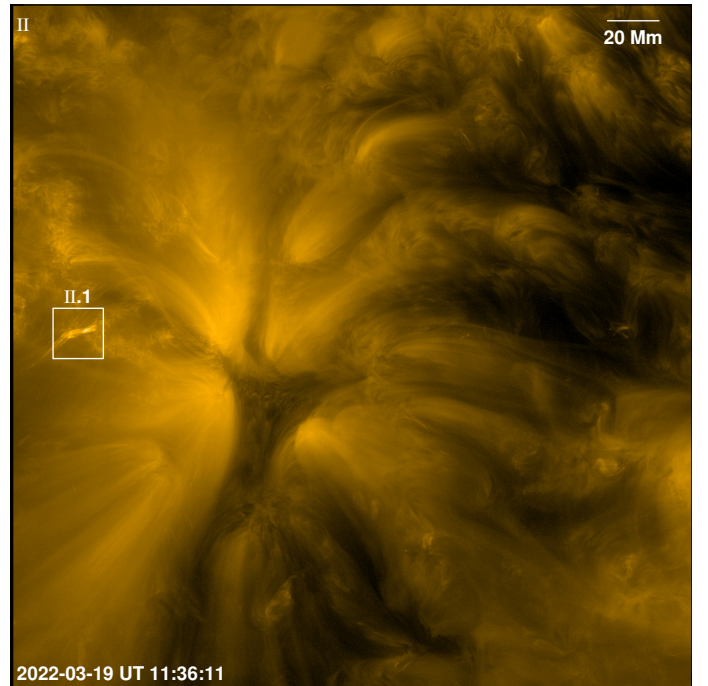


**Fig. A.5.** Decaying active region AR12967 (AR-II) observed by EUV/HRI<sub>EUV</sub> on 2022 March 19. The white box II.1 outlines a coronal jet event with compact braided loops at its base. The evolution of this loop system is further elaborated in Fig. 5. The intensity of the displayed image is on a log-scale. North is roughly up. See Table 1, Sect. 2 and the Appendix A for details.



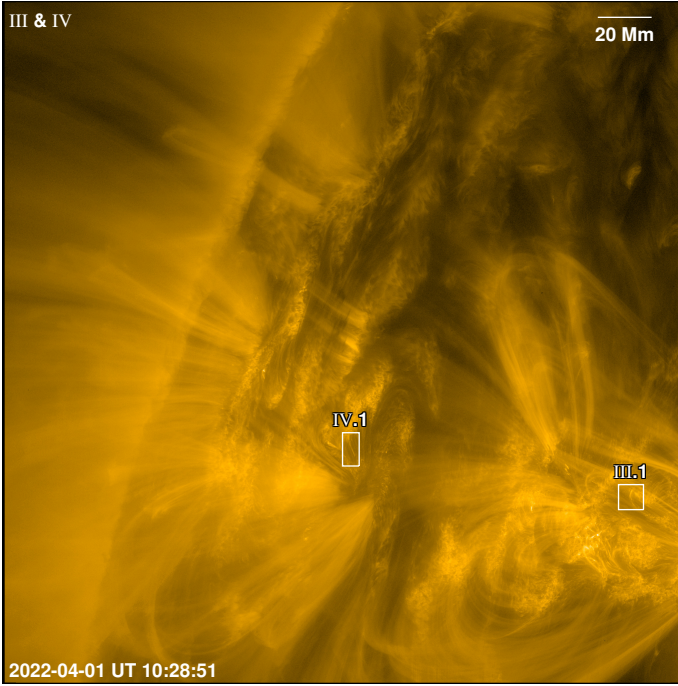


**Fig. A.6.** A pair of active regions AR-III (western) and AR-IV (eastern) observed by EUV/HRI<sub>EUV</sub> on 2022 April 01. Boxes III.1 (partially covering AR12975) and IV.1 (partially covering AR12976) are further displayed in Figs. A.7 and A.8, respectively. The intensity of the displayed images is on a log-scale. North is roughly up. See Table 1, Sect. 2 and the Appendix A for details.

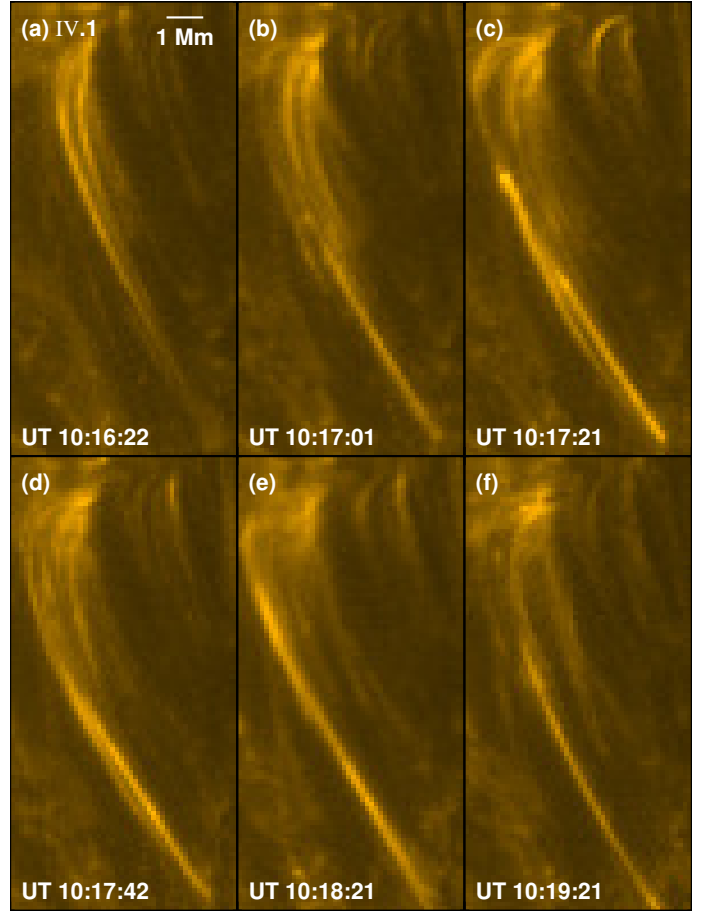


**Fig. A.8.** Same as Fig. A.7, but plotted for region AR-IV.1 (AR12976) marked in Fig. A.6. Intensity of the displayed images is on a square-root-scale. See the Appendix A for details. Animation of this figure is available online.

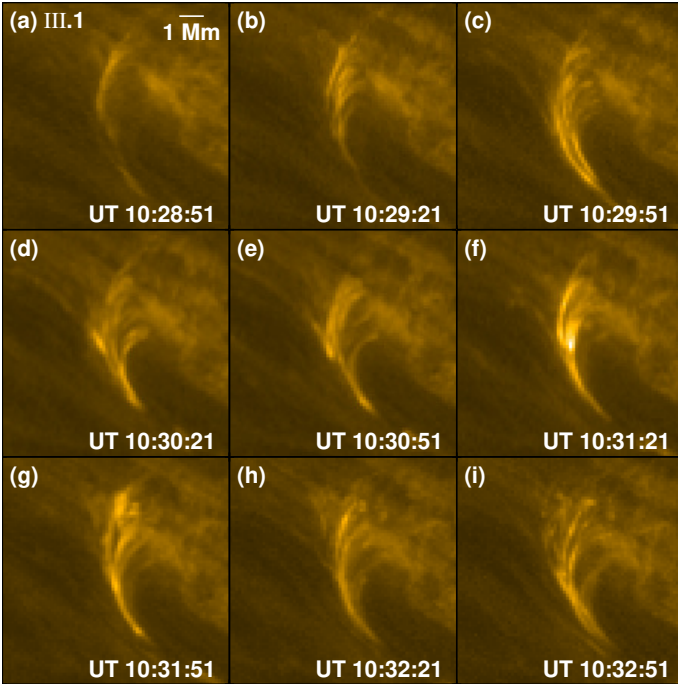


**Fig. A.7.** Zoomed-in view of region AR-III.1 marked in Fig. A.6. Panels (a)–(i) show the evolution of braided loops over filamentary structures in AR12975. Intensity of the displayed images is on a square-root-scale. See the Appendix A for details. Animation of this figure is available online.

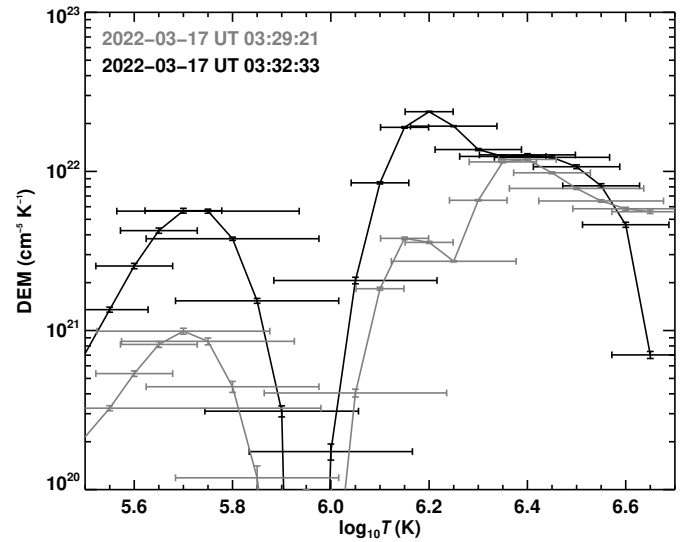


**Fig. B.1.** Thermal diagnostics of the braided loops. We plot the DEM as a function of temperature for the SDO/AIA mean intensities derived from the braided loops (i.e. the black box on AIA panels in Fig. 2). The gray and black curves are computed at time-stamps overlaid on the plot. The vertical error bars correspond to  $1\sigma$  errors in the DEM, while the horizontal bars indicate the energy resolution of the regularized inversion technique. See the Appendix B for a discussion.



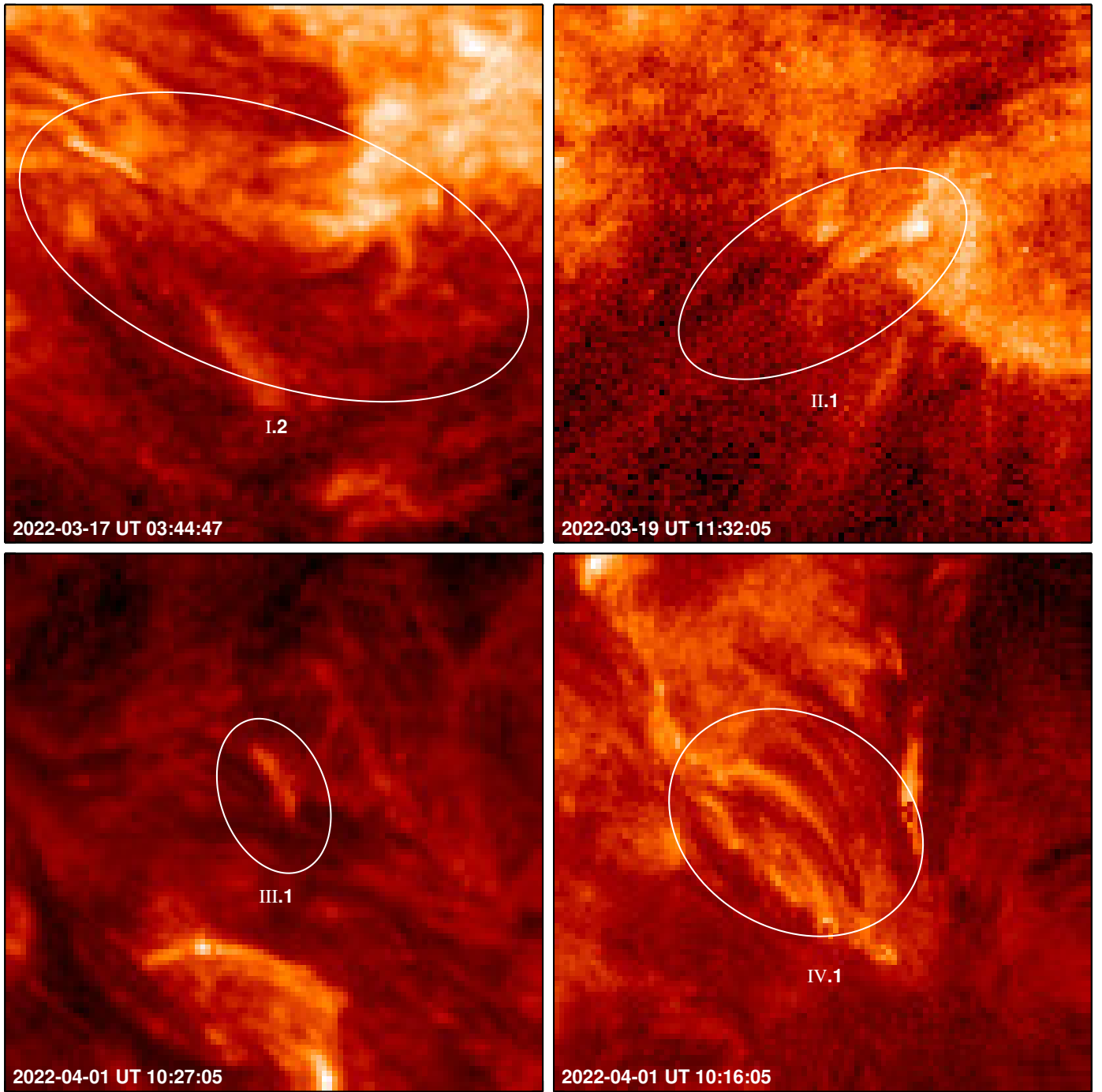


**Fig. C.1.** Chromospheric filamentary structures. The four panels show the SDO AIA 304 Å snapshots of four of the coronal braids (as labeled in each panel). The ellipses identify the chromospheric filamentary structures associated with the  $\text{HRI}_{\text{EUV}}$  braids. Each panel covers a field of view of  $44 \text{ Mm} \times 44 \text{ Mm}$ . North is up. See the Appendix C for a discussion.